Probing the local radiative quenching during the transition from a non-smoking to a smoking laminar coflow ethylene/air non-premixed flame

Jérôme Bonnety, Augustin Guibaud, Renaud Jalain, Alexis Matynia, Jean-Louis Consalvi, Fengshan Liu, Guillaume Legros

Version of Record: https://www.sciencedirect.com/science/article/pii/S0010218019300604
Manuscript_d41b3cb74b1fb8389cee072f0607e741

Probing the local radiative quenching during the transition from a non-smoking to a smoking laminar coflow ethylene/air non-premixed flame

Jérôme Bonnety[a], Augustin Guibaud[a], Renaud Jalain[a], Alexis Matynia[a], Jean-Louis Consalvi[b], Fengshan Liu[c], Guillaume Legros[a,*]

[a] *Sorbonne Université, Centre National de la Recherche Scientifique, UMR 7190, Institut Jean Le Rond d'Alembert, F-75005 Paris, France*
[b] *Aix-Marseille Université, IUSTI/UMR CNRS 7343, 5 rue E. Fermi, 13453 Marseille Cedex 13, France*
[c] *Measurement Science and Standards, National Research Council of Canada, Ottawa, Ontario, Canada.*

Abstract

This paper experimentally documents the transition from the "closed-tip" flame configuration to the "open-tip" one that a laminar axisymmetric coflow ethylene/air non-premixed flame experiences with increasing the fuel flow rate at the smoke point in terms of soot temperature and volume fraction distributions. To this end, the two-dimensional soot temperature and volume fraction fields are measured by the two-color Modulated Absorption/Emission (2C-MAE) technique. The MAE setup has been specifically extended to a third spectral range centered at a lower wavelength (405 nm).

*Corresponding author
Email addresses: jerome.bonnety@upmc.fr (Jérôme Bonnety), augustin.guibaud@upmc.fr (Augustin Guibaud), renaud.jalain@upmc.fr (Renaud Jalain), alexis.matynia@upmc.fr (Alexis Matynia), jean-louis.consalvi@univ-amu.fr (Jean-Louis Consalvi), Fengshan.Liu@nrc-cnrc.gc.ca (Fengshan Liu), guillaume.legros@dalembert.upmc.fr (Guillaume Legros)

With this new 3C-MAE technique, information on the level of scattering attributed to soot particles can be obtained. The experimental investigations are combined with radiative heat transfer computations to gain a comprehensive understanding of the radiative quenching of soot oxidation that happens at the flame tip responsible for soot release from the flame at the smoke point. In addition, the field of spectral scattering coefficient at 405 nm can be estimated, confirming that the non-scattering approximation is valid within the context of radiative models in this kind of flame. As a result, numerical simulations implementing radiative models without scattering should be able to decently capture the transition at the smoke point. Since the simulation of such a transition is crucial to the control of carbonaceous nanoparticles release process from flames, an original contribution of the present paper to this challenge is the supplemental material that contains the measured two-dimensional fields of both soot temperature and volume fraction measured.

Keywords: Soot, non-premixed flame, smoke point, radiative quenching, optical diagnostics

---

1. Introduction

Energy production and its impacts are traditionally the focus of combustion science. As a result, strategies aiming at soot emissions mitigation and suppression [1, 2] have been especially emphasized for the last two decades. Following these efforts, significant insights into the understanding of soot formation, growth, and oxidation have been achieved, using both advanced experiments [3, 4] and numerical modeling [5–8] that open the way to the optimization of "soot-free" processes. Conversely, steady smoking

flames can also be considered as very reproducible generators of carbonaceous nanoparticles with characteristics (size, crystallinity, morphology) that are to be appropriately controlled [9–11]. As an illustration, the configuration of the axisymmetric coflow non-premixed burner has been widely employed for commercial production of flame-made nanomaterials [10, 11].

One of the major challenges shared by both targeted configurations lies in the accurate control of the conditions that lead to soot release to the atmosphere. Recently, Abboud et al. [12, 13] showed that the size of soot aggregates released by a steady atmospheric axisymmetric coflow non-premixed flame can be controlled, both in terms of mean and distribution, through the addition to the fuel stream of properly selected oxygenated compounds. However, the oxidative reactivity of soot sampled was found to decrease when increasing a given oxygenated compound content. This trend was correlated with lower amorphous carbon concentration in the soot sampled. As a result, the authors emphasized the need for further investigations on the conditions at the flame tip, through which soot is released. Further downstream, the soot related processes are frozen, especially due to the dramatic temperature drop through thermal radiation transfer [5]. As a result, controlling the flame characteristics causing soot emissions requires fine understanding of the processes leading to soot release itself.

Originally introduced to quantify the soot production propensity of any fuel [14], the smoke point concept has been deeply explored [15–17], suggesting that an axisymmetric coflow laminar non-premixed flame quenches at its tip due to radiative heat losses at fixed critical conditions in soot concentration and temperature. Flames can be "closed-tip" (below the smoke

point) when soot is consumed before these critical conditions are attained, or "open-tip" (beyond the smoke point) if quenching of soot oxidation occurs before soot is fully consumed, soot particles being released through the open flame tip.

Soot production is one of the most complex combustion related phenomena since it stands at the heart of the couplings among chemical kinetics, polycyclic aromatic hydrocarbon (PAH) formation, nucleation, particle dynamics, energy and radiative transfer. As a result, high performance computing including sophisticated models of soot formation and oxidation has been extensively developed for the last two decades, delivering numerical simulations that can decently predict the local soot concentrations in flames [5, 6, 18–21]. As the integration of highly detailed soot models into CFD codes remains intractable for most of today's computational resources, less computationally demanding semi-empirical soot production models have to be used in multidimensional problems. Among these, some produced fair results, interestingly using the smoke point characteristics as an input to the soot formation models [19, 20].

In contrast, few studies devoted to the fine numerical simulation of the transition from the "closed-tip" flame configuration to the "open-tip" one. To this end, Liu et al. [5] extended a CFD code that incorporates both simplified soot chemistry and radiative transfer models. These authors needed to introduce two temperature-dependent correction factors in the soot oxidation schemes to successfully simulate the smoke point for a given experimental configuration, i.e. to properly reproduce the quenching of soot oxidation at the flame tip. The authors indicated that the exact physical and chemical

processes associated with the modified soot oxidation rates were not fully understood and no guarantees can be made that the model would be accurate in other configurations. Thus, documenting the soot and temperature characteristics at the vicinity of the smoke point conditions could provide insights into the understanding of the phenomena governing the transition. As an illustration of the synergy that experimental and numerical studies can produce, Kashif et al. [22] showed experimentally that as toluene is added to isooctane in the fuel stream of their non-premixed laminar axisymmetric methane flame, additional soot production is observed compared with that obtained with the same toluene addition to n-heptane. The subsequent numerical simulations by Consalvi et al. [23] then helped identify some specific chemical pathways that govern this phenomenon. Within the context of smoke point, development of the modeling capability to predict the smoke point condition would make it a very useful tool. However, the prediction of smoke point poses a severe challenge to the capability and integrity of soot models.

The present study focuses on providing an experimental characterization of soot related fields under conditions around the smoke point of a steady laminar axisymmetric ethylene/air non-premixed flame. The experimental setup implemented by Jocher et al. [24] is used. The flame is established over the Santoro burner that has been well documented in the literature, especially with respect to soot [22, 25–30]. With this configuration, soot temperature measurements using thermocouples [28], soot volume fraction, particle size, and number density [29], and morphology based on analysis of transmission electron microscope (TEM) images of thermophoretically sampled soot [30]

have already been documented at the vicinity of the smoke point. While these pioneering studies delivered significant insights to the understanding of the smoke point phenomenology, non-invasive optical techniques can now probe the flames of interest with relatively high spatial resolution. Here, the fields of both soot temperature and volume fraction covering the whole sooting region in the flame are measured by the two-color Modulated Absorption/Emission (2C-MAE) technique developed by Legros et al. [31]. As an original contribution to the optical diagnostics, a third laser beam operating at a wavelength of 405 nm has been incorporated to estimate the distribution of local scattering coefficient attributed to soot. Doing so, the upgraded three-color MAE (3C-MAE) is expected to provide an experimental assessment of radiative heat transfer models in flames that usually assume negligible contribution of scattering [5].

2. Experiments and diagnostics

Figure 1 displays the schematic of the upgraded experimental setup that now allows both soot temperature and volume fraction to be mapped simultaneously in axisymmetric flames by 2C-MAE and incorporates a third beam produced by a blue continuous wave (CW) laser operating at 405 nm.

2.1. Flames

The non-premixed flames are established at constant room temperature of 295K over an atmospheric axisymmetric coflow burner, identical to the one described by Santoro et al. [29]. With this burner configuration, the sooting behaviors of a wide range of fuels, in particular ethylene, have been extensively documented in the literature [5, 22, 25].

Ethylene (C_2H_4) flows through the vertical central brass duct, which has an inner diameter of injection d_F of 11 mm. The coflowing air is introduced into a concentric brass cylinder of 102 mm inner diameter. Two Bronkhorst EL-FLOW mass flow controllers enable the variation of both the air and ethylene flow rates. All gases come from high-purity gas cylinders (99.9% stated purities). Further details about the characteristics of the present burner can be found in earlier publications [32–34].

In the following, the vertical burner's axis of symmetry is referred to as Oz and its origin is located at the nozzle exit plane, defining the height above the burner (HAB). The cross-stream coordinate is r, which is the distance from the axis of symmetry.

The study concerns the transition from non-smoking to smoking flame around the smoke point. To this end, the ethylene flow rate increased gradually from 0.191 ± 0.003, to 0.210 ± 0.003, 0.229 ± 0.003, 0.239 ± 0.003, and finally to 0.248 ± 0.004 L.min^{-1}. These conditions are reported in Tab.1 to identify flames A-E, respectively.

The transition was expected to happen for an ethylene flow rate between 0.265 and 0.276 L.min^{-1} if the air flow rate is set to 43 L.min^{-1} [35]. However, for this air flow rate and ethylene flow rates higher than 0.240 L.min^{-1}, the very flame tip starts experiencing a 12 Hz flickering as revealed by the optical diagnostics delivering 45 fields per second. The 10 Hz LII measurements by Shaddix and Smyth [35] may have blurred this phenomenon. As a result, the air flow rate is here kept constant at 60 ± 0.4 L.min^{-1} which makes flames A-E all laminar and steady. For this air flow condition, flame E is smoking while flames A-D are not.

2.2. 3C-MAE

The basics of the 2C-MAE technique that have been extensively detailed in Ref. [31] are here briefly recalled. This technique is shown to provide simultaneously up to 45 two-dimensional fields per second of soot temperature and volume fraction in axisymmetric laminar non-premixed flames with uncertainty levels lower than $\pm$ 50K and $\pm$ 0.2 ppm, respectively [26, 27], and a spatial resolution of 100 μm. These features have been improved as compared to those evaluated in Ref. [31], especially in terms of spatial resolution, due to the use of more sensitive cameras specified below.

Within the red spectral range (centered at λ_1=645 nm) and the near infrared one (centered at λ_2=785 nm), the flame is considered an emitting, absorbing, but non-scattering medium. For the laminar coflow ethylene flames studied, the flame radiative spectrum in the visible is governed by the continuum radiation from soot [36]. This is particularly true in the upper part of the visible spectrum. In addition, absorption by soot particles produced in these flames is shown to be at least one order of magnitude higher than scattering at longer wavelength in the visible spectrum [37]. In such a configuration, the Radiative Transfer Equation (RTE) that models the transfer of the radiative intensity can be integrated along the optical pathways followed by the collimated laser beam inside the flame (see Fig. 1). When the laser beam is off, the energy accumulated on a pixel of a camera during the exposure time is mainly attributed to the steady impinging flux emitted by the flame, which can then be imaged within a spectral range located around a wavelength λ provided that the camera is mounted with a narrow band filter. When the laser is on (see the insets in Fig. 1), the energy accumu-

lated on the same pixel is complemented by the transmitted energy of the non-coherent collimated laser beam. Imaging consecutively the flame with then without the laser beam allows the difference between both frames to be only connected to the spectral extinction coefficient field β_λ, that is the spectral absorption coefficient field κ_λ provided that the spectral range is adequately selected as discussed below. As the information is integrated over the line-of-sight, the measurements need to be combined with a subsequent deconvolution procedure to compute the local fields $\kappa_\lambda(r,z)$. To this end, an onion-peeling method combined with a Tikhonov regularization is employed. The soot volume fraction field $f_v(r,z)$ can then be inferred. The Mie theory allows κ_λ to be related to f_v, assuming that soot particles are within the Rayleigh limit [33]:

$$f_v(r,z) \;=\; \frac{\lambda\,\kappa_\lambda(r,z)}{6\,\pi\,E(m)} \tag{1}$$

where $E(m)$ is a function of the complex refractive index m of soot. For a matter of consistency with the radiative heat transfer computations performed in the following, the model predicting the spectral dependence of m_λ proposed by Chang and Charalampopulos in ethylene flames [38] is selected.

The frame captured in the absence of the laser beam is then processed in a similar way to provide the local spectral emission rate $\kappa_\lambda B_\lambda(r,z)$, where B_λ is the spectral blackbody radiative intensity at the local temperature T given by the Planck's law [31]. As a result, $B_\lambda(r,z)$ can be extracted as the ratio $(\kappa_\lambda B_\lambda)/\kappa_\lambda$. Conducting these measurements within two spectral ranges centered at λ_1 and λ_2 then allows the field of $B_{\lambda_2}/B_{\lambda_1}$ to be computed. The field of soot temperature $T(r,z)$ can finally be inferred from a lookup table that provides T as a function of the ratio $B_{\lambda_2}/B_{\lambda_1}$

It is worth noticing that the procedure deriving the soot spectral emission rate field intrinsically includes soot self-absorption along the line-of-sight. In addition, the determination of the soot temperature by the 2C-MAE technique does not require any model for the spectral dependence of the soot refractive index as the fields of κ_λ are measured within both spectral ranges of detection. On the opposite, the determination of soot temperature by any conventional multi-wavelength pyrometry requires such a model [39, 40], knowing that soot refractive index is a quantity that is a topic of ongoing debate as large discrepancies are reported in the literature [41, 42].

The 2C-MAE setup has been extended to enable the new 3C-MAE implementation as shown in Fig. 1. The additional beam is produced by another CW laser operating at λ_3= 405 nm (+5nm/-5nm) and combined with the other two. An optical setup then constitutes a homogeneizing beam expander that provides with a 100 mm diameter 3-color collimated beam. New lenses have also been incorporated to enlarge the beam, which now encompasses the whole smoking flame E. The telecentric configuration of the collection setup finally enables the imaging of every beam on an associated 16-bit PCo SCMOS progressive scan monochrome camera with a spatial resolution of 40 μm ($\pm$ 5 μm) for the projected data. Details about the sophisticated optical arrangement that is especially required to combine laser beams and image them on different cameras can be found in Ref. [31].

Although soot characteristics dominate the radiative properties at the three spectral bands in the sooting flames investigated, gaseous spectral bands are present in sooting flames in the visible spectrum. With regard to emission, the bands selected to operate the 3C-MAE technique stand away

from the main emission bands by gaseous species, especially those of the CH radicals at 431 nm and C_2 (Swan bands between 440 nm and 570 nm). With regard to absorption, the detection limit is especially to be discussed in the light of the absorption that can be attributed to a major species among the pool of PAHs, such as pyrene (PY). The detection limit of the MAE technique is evaluated at 0.5 ppm [31], leading to $\kappa_{\lambda_3}^{det} \sim 6.5$ m^{-1}. Should pyrene contribute to $1/10^{\text{th}}$ of this absorption level, measurements of pyrene absorption at λ_3 by Niko et al. [43] lead to [PY] ~ 0.32 mol.L^{-1}. This is 7 orders of magnitude higher than the peak molar concentration of pyrene simulated by Liu et al. in very similar ethylene/air flames [44]. Besides, it is worth mentioning that no absorption by pyrene was measured beyond 600 nm by Niko et al. To be thorough, such a consideration should be extended to all PAHs. However, this would especially require the knowledge of all these PAHs' absorption cross-sections, which are only partially available today. In addition, any kinetic model incorporated to a CFD code may lead to large uncertainties on the production rates of minor species, such as PAHs. As a matter of fact, more attention needs to be paid especially in weakly sooting flames where the absorption by PAHs may significantly compete with that by low levels of soot volume fraction. In contrast, high levels of soot volume fraction are present in the major part of the sooting flames investigated here. For these reasons, absorption by gaseous species is neglected within the framework of the present study for the three spectral ranges probed by the 3C-MAE technique.

The insets in Fig. 1 show the line-of-sight images of the flame captured by the camera to illustrate the variation of the balance between extinction and

emission in the visible spectrum. While emission dominates within the near infrared spectral range (c), extinction largely overcomes it at the shortest wavelength (a). This clarifies the apparently weak luminosity of the flame within the red spectral range (b) where both phenomena are important. The particle size parameter $\pi D/\lambda$, where D is a characteristic optical soot particle diameter, plays a major role in this balance. As an illustration, the Mie theory predicts that for a monodisperse population of spherical particles, both absorption and scattering cross sections decrease with increasing wavelength, the decreasing rate being higher for the latter. As a result, scattering by soot is usually considered negligible as compared to absorption at long wavelength in the visible spectrum, as mentioned earlier [37]. In other words, the signals collected at a shorter wavelength, say λ_3, presumably convey information about scattering, therefore potentially particle size.

2.3. Radiative heat transfer computations

The divergence of the radiative flux at every location where soot volume fraction and temperature are measured can be computed. To do so, the RTE is solved in its non-scattering formulation for the radiative intensity I_λ using the Finite Volume Method proposed by Chui et al. [45] for axisymmetric coordinates with a 12x16 angular mesh. For the laminar ethylene/air flames investigated, radiation by soot was found to prevail over that by gaseous species over the spectrum relevant to thermal radiation at flame temperatures [36]. Consequently, the contributions of gaseous products (mainly CO_2 and H_2O) to radiative heat transfer can be neglected. At every location, the

divergence of the radiative flux is expressed as follows:

$$\nabla \cdot \mathbf{q}^R = \int_0^\infty \left(4\,\pi\,\kappa_\lambda\,B_\lambda - \kappa_\lambda \int_{4\,\pi} I_\lambda\,d\Omega \right) d\lambda \tag{2}$$

Ω being the solid angle.

Thus, the numerical computations require a model for the spectral dependence of κ_λ, or equivalently for m_λ when f_v is known (see Eq. (1)). The model of Chang and Charalampopulos [38] is selected for the present study.

Among the major assumptions needed to arrive at Eq.(2), the soot scattering coefficient σ_λ is neglected as compared to its absorption one κ_λ. This specific issue might be assessed using the experimental fields of attenuation measurements at shorter wavelength λ_3.

3. Results and discussion

3.1. Soot volume fraction and temperature fields

The fields of soot volume fraction and temperature are shown in Fig. 2, together with the profiles of the mean flame cross-section integrated soot volume fraction $F_v(z)$, defined as follows:

$$F_v(z) = \frac{4}{\pi\,d_F^2} \int_0^{d_F/2} 2\,\pi\,r\,f_v(r,z)\,dr \tag{3}$$

d_F=11 mm being the effective diameter of injection. Thus, $F_v(z)$, referred to as mean soot volume fraction in the following, appears as an evaluation of the actual soot load at a given HAB in the flame.

As the fuel flow rate is increased from flame A to flame E, more soot is produced in the flame, as indicated by the monotonic increase in the peaks of both soot volume fraction and mean soot volume fraction, referred to as

$f_{v,max}$ and $F_{v,max}$, respectively. Concomitantly, the radial location r_{max} of $f_{v,max}$ is not significantly affected and remains on the wing. In contrast, the axial location z_{max} of $f_{v,max}$ first moves downstream from flame A to flame D then moves slightly upstream for flame E (see horizontal yellow lines). This reversed trend may be due to the conditions at smoke point that penalize soot oxidation at the upper part of the flame as the fuel flow rate is increased from flame D to flame E.

The bases of all the five flames A-E exhibit very similar soot temperature distributions, with the hotter region appearing on the flame wing region, where relatively high levels of soot volume fraction are located close to the flame sheet on its rich edge. From flame A to flame E, the relatively colder region spreads over downstream and a trident shape gradually appears (see the clear splitting of the central tip and the top of the wing from flame A to flame D, as evidenced by the white dotted contours on the soot volume fraction fields). This is in agreement with the reported phenomenology of the smoke point [15, 16] where the conditions close to the centerline region around the flame tip do not allow complete oxidation of soot. As a result, soot is released through the tip of the smoking flame E (see the plateau of non-zero value in the upper profile of F_v for flame E in Fig. 2).

Figure 3 supports these comments in a more quantitative way, showing the evolution of the measurements population in the soot temperature/volume fraction plane. The red dots identify the measurements in the region of the flame located beyond z_{max}. Consequently, these especially contribute to the peak soot volume fraction that is right and down shifted from flame A to flame E, as evidenced by the monotonic decrease of temperature $T(f_{v,max})$

(see on the right of Fig. 3) away from the adiabatic flame temperature of ethylene burning in air (2620K). This trend manifests that at the location of the peak soot volume fraction, soot experiences conditions that could tend to reduce soot oxidation. It is evident from Fig. 3 that the regions of lower temperature and lower soot volume fraction above z_{max} (red dots) increase significantly from flame A to flame E, which is consistent with the enlarged sooting region in the upper part of the flame with increasing the fuel flow rate shown in Fig. 2.

Since the simulation of the transition from non-smoking flames to smoking ones is crucial to the control of carbonaceous nanoparticles release process from flames, the supplemental material contains the two-dimensional fields of both soot temperature and volume fraction measured in flames A-E, as an original experimental database for the validation of numerical codes.

3.2. Local radiative quenching

The evolution of the population along the transition shown in Fig. 3 is expected to significantly affect the radiative balance in the flame, which in turn has been shown to strongly influence soot formation and oxidation processes [5]. Figure 4 displays the fields of the divergence of the radiative flux computed as specified in Section 2.3. Like for $f_{v,max}$, the region of higher soot emission shifts downstream from flame A to flame D, as evidenced by the downstream shift of the trailing edge of the contour delineated by the white solid line.

From flame D to flame E, this region keeps spreading over downstream. Meanwhile, the soot load keeps growing (see the monotonic increase in $F_{v,max}$ on the leftmost profiles of F_v in Fig. 2) while the location of $f_{v,max}$ starts

to shift upstream (see the horizontal yellow lines in Fig.4) and experiences lower temperature (see $T(f_{v,max})$ in Fig. 3). At some point between flame D and flame E, soot is released through the flame tip, as shown in the upper profile of F_v that tends towards a non-zero constant value for flame E in Fig. 2. Due to the significantly lower levels of the radiative balance at the flame's trailing edge, the fields of radiative balance in Fig. 4 are highly noisy within this region. As a result, it is challenging to identify the contours there. For this reason together with legibility, only the outer locations of the radiative balance at 5% of the respective peak value of the flame are connected by a white dotted line for flames D and E to highlight the transition from a closed distribution of the radiative balance in flame D to an open one in flame E. Thus, although soot oxidation seems to vanish in flame E, or at least is sufficiently weakened to allow soot to escape the flame, radiative losses by soot do not. The radiative heat losses may then contribute to quench locally soot oxidation at the flame tip, as numerically predicted by Liu et al. [5].

To elaborate the local effect of the global radiative losses on soot oxidation in the upper part of the flames, the relative soot consumption rate $1/F_{v,max}\, dF_v/dz$ can be correlated at every z beyond the location $z_{F_{v,max}}$ of $F_{v,max}$ with the radiative power attributed to soot and cumulated between $z_{F_{v,max}}$ and z. Figure 5 displays the trend lines illustrating such correlations in flames A-E. The present measurements do not enable the discrimination between soot formation and oxidation rates. However, beyond $z_{F_{v,max}}$, the soot load budget is dominated by soot oxidation, as shown in Fig. 2 by the relatively dramatic decay of F_v. As the flow is mainly directed upward at the flame tip, following a trend line in Fig. 5 from the left to the right can

be considered a way to track the radiative losses that the initial soot load $F_{v,max}$ will experience within its oxidation process. For each of flames A-D, this soot load has been fully consumed when $1/F_{v,max}\, dF_v/dz$ finally vanishes at the flame tip (see the color circles at the end of these lines). In contrast, a non-negligible level (F_v=0.18) escapes through the tip of flame E while the non-vertical tangent at the end on the trend line reveals that further radiative losses attributed to the escaping soot will contribute to the flame radiative power downstream the location where $1/F_{v,max}\, dF_v/dz$ vanishes.

For all the flames, the first part of the trend line shows that the intensification of the oxidation process along z is combined with an increasing cumulated radiative power. Beyond the peak consumption rate, the rate of late oxidation decreases while a smaller contribution is then added to the total cumulated radiative power achieved at $1/F_{v,max}\, dF_v/dz$=0, which corresponds to the low radiative balance in the centerline region close to the flame tip in Fig. 4.

Approaching the transition, i.e. from flame A to flame D, the intensification of the oxidation process along z is associated with higher and higher levels of cumulated radiative power. This tendency contributes to weaken the oxidation process, i.e., to reduce the slope of the first part of the trend line. This is further supported examining the locations of $F_v = 0.74$ (see the purple circles) from flame A to flame D. At this equivalent level of soot load, the cumulated radiative power is higher and higher, which causes more adverse conditions for the full oxidation of the remaining soot load. Interestingly, the decrease of the aforementioned slope stops from the non-smoking flame D to the smoking flame E. Given the very small increase of the slope,

talking about a trend reversal is here premature.

Similarly, the second part of the trend lines, where the consumption rate decreases and finally vanishes, is shifted towards higher and higher levels of cumulated radiative power from flame A to flame D. Now, the trend reversal from flame D to flame E reveals. At the location of $F_v = 0.62$ (see the green circles), the cumulated radiative power for flame E is larger enough than that for flame D to weaken the oxidation to a rate that will ultimately prohibit the full consumption of the remaining soot load in flame E. This tendency thus contributes to the local quenching of the soot oxidation processes.

To the authors' knowledge, the above characterization is the first experimental assessment corroborating the findings by earlier studies that qualitatively revealed the radiative quenching of soot oxidation leading to the smoke point [15, 16].

3.3. Discussion

Although the actual spectral dependence of the soot refractive index is beyond the scope of the present study, the sensitivity of the above insights to the selected spectral dependence given by Chang and Charalampopoulos can be assessed using an alternative law. This was calibrated here with the measurements of the soot refractive index by Dalzell and Sarofim [46] by analogy with the Chang and Charalampopoulos' law. New fields of radiative balance could then be computed. For legibility, the associated contour is only shown for flame E in Fig. 4 (see the circles). Admittedly, the level of the radiative balance changed with the selected law, with a peak radiative balance of 50.8 MW/m^3 with the Chang and Charalampopoulos' law and 67.1 MW/m^3 with that of Dalzell and Sarofim for flame E. Nevertheless, the

contours are hardly affected. Consequently, the selection of the aforementioned spectral dependence does not alter the understanding gained in this study qualitatively.

To further address the level of radiative model required to reproduce properly the quenching at the tip of the sooting flame, a methodology to evaluate the distribution of the local scattering coefficient at λ_3 is discussed below. With the optical setup shown in Fig. 1, the measurement of the laser extinction β_λ is conducted at zero degree incidence for all spectral ranges. Therefore, extinction is the result of the superimposition of both absorption and single-scattering, due to the fields of κ_λ and σ_λ, respectively, along the line-of-sight. While the contribution to extinction by scattering at 785 nm can be considered negligible, i.e. $\beta_{\lambda_2} \approx \kappa_{\lambda_2}$, as the size parameter is relatively low [5], the measured β_{λ_3} is likely to contain non-negligible contribution by σ_{λ_3}.

To verify the above statement, the lower row in Fig. 6 displays the evolution of the ratio $\beta_{\lambda_3}^{peak}/\kappa_{\lambda_2}^{peak}$ along z for all flames, where the superscript peak indicates the peak measured at HAB z. The consistency of every ratio shown is here represented by the opacity of the circle, which is proportional to both relative levels of $\kappa_{\lambda_2}^{peak}(z)$ and $\beta_{\lambda_3}^{peak}(z)$ (1 (black): the maximum value of $\kappa_{\lambda_2}^{peak}(z)\,\beta_{\lambda_3}^{peak}(z)$ in the flame considered; 0 (white): $\kappa_{\lambda_2}^{peak}(z)\,\beta_{\lambda_3}^{peak}(z)$=0). As shown by Michelsen et al. [47], for a given burner configuration and a given fuel, the ratio $\kappa_{\lambda_3}/\kappa_{\lambda_2}$ is essentially a function of soot maturity, i.e. soot residence time in the flame. The ratio $\beta_{\lambda_3}^{peak}/\kappa_{\lambda_2}^{peak}$ in the lower parts of the five flames A-E remains here very similar. Yet, in this kind of flames, the residence time is mainly governed by buoyancy, therefore the temperature

field. For this reason, the strong similarity among the lower evolutions of $\beta_{\lambda_3}^{peak}/\kappa_{\lambda_2}^{peak}$ in the lower part of the flames is in agreement with that of the temperature fields at the bases of the flames (see Fig. 2). In addition, beyond $z/d_F \approx 4$, all profiles converge towards the same constant value. Interestingly, this value is close to that predicted by Michelsen et al. [47]. Through the study of mature soot released by ethylene flames, these authors extracted a law in $\lambda^{-0.83}$ that the absorption cross-section follows, deviating from the commonly assumed law in λ^{-1}. The upper parts of the $\beta_{\lambda_3}^{peak}/\kappa_{\lambda_2}^{peak}$ profiles tend to evidence the presence of mainly mature soot beyond $z/d_F \approx 4$ for all flames investigated.

The upper row in Fig. 6 illustrates the method that can now yield the evaluation at first order of the local scattering coefficient. Given the above finding, the absorption coefficient at λ_3 can be inferred from that measured at λ_2, as follows:

$$\kappa_{\lambda_3} = (\lambda_3/\lambda_2)^{-0.83}\,\kappa_{\lambda_2} \tag{4}$$

Thus, a profile of measured κ_{λ_2} can be converted into a profile of estimated κ_{λ_3} that is theoretically free of single-scattering (red line). Then the local scattering coefficient σ_{λ_3} (black line) is evaluated as the difference between the profile of measured β_{λ_3} (blue line) and the profile of estimated κ_{λ_3}.

The shape of σ_{λ_3} looks consistent with the conditions in this kind of flame. At the vicinity of the axis, the particles experience rich conditions within relatively long residence times. As a result, they exhibit quite large diameter and/or level of agglomeration, which enhances the soot scattering. Moving outwards, the profile of σ_{λ_3} vanishes as oxidizing conditions prevail, leading to the decrease in particle size, therefore the scattering level. This

observation especially matches the profiles of particle diameters measured by Steinmetz et al. in the upper part of their ethylene/air non-premixed flames (see Fig. 7 in Ref. [48]). It is worth mentioning that this latter finding further supports the relevance of the location selected to evaluate the ratio $\beta_{\lambda_3}/\kappa_{\lambda_2}$ in Fig. 6, i.e., at the peak β_λ. Indeed, due to the inward onion-peeling procedure that is conducted along the 3C-MAE processing, the parts of the fields inferred from signals imaging the outer rings of the flame, where the aforementioned peaks occur, can be considered less affected by scattering bias.

As evidenced by the bumpy profile of σ_{λ_3} in Fig. 6, the level of the inferred local scattering is hardly higher than that of the noise. As a result, values of σ_{λ_3} will be constrasted with those of β_{λ_3} in terms of mean quantities. By analogy with Eq.(3), these are defined as follows:

$$\overline{X}(z) = \frac{4}{\pi\, d_F^2} \int_0^{d_F/2} 2\,\pi\, r\, X(r,z)\, dr \tag{5}$$

X being either σ_{λ_3} or β_{λ_3}.

Figure 7 displays the evolutions with HAB of both $\overline{\sigma}_{\lambda_3}$ (red lines) and $\overline{\beta}_{\lambda_3}$ (black lines) within flames A-E beyond the location where soot can be considered mature, i.e. $z/d_F > 4$. Along the x-axis, two different scales by a factor of 10 are selected for the lower and upper axes, associated with β_{λ_3} and σ_{λ_3}, respectively. On every curve, the solid line identifies the part located within the region of the flame that covers 90% of the radiative power attributed to soot (see the white contours in Fig. 4).

For all flames, $\overline{\sigma}_{\lambda_3}$ first increases with HAB while $\overline{\beta}_{\lambda_3}$ monotically decreases. Then $\overline{\sigma}_{\lambda_3}$ exhibits a peak. This observation is consistent with the measurements of particle diameter by Steinmetz et al [48], who found the

maximum particle diameter beyond the location of maximum F_v. Thus, the inner soot particles keep on growing in size while soot oxidation globally overcomes soot formation, especially in the outer region of the flame.

For non-smoking flames A-D, $\overline{\sigma}_{\lambda_3}$ finally vanishes at the flame tip, so does $\overline{\beta}_{\lambda_3}$, revealing that all soot is oxidized. For smoking flame E, $\overline{\sigma}_{\lambda_3}$ also decreases at the flame tip but, in contrast, does not vanish and tends towards a plateau, just like $\overline{\beta}_{\lambda_3}$ and F_v (see Fig. 2). Thus, soot related processes look to be quenched at the flame tip, which releases soot with no significant modification in load and possibly morphology beyond the quenching location. This observation might be of interest for the control of released soot characteristics.

In addition, as compared to the level of $\overline{\beta}_{\lambda_3}$, $\overline{\sigma}_{\lambda_3}$ remains significantly weak, never exceeding 20% of $\overline{\beta}_{\lambda_3}$, even at the upper edge of the main emitting region (see the top ends of the solid lines in Fig. 7). As the ratio $\sigma_\lambda/\beta_\lambda$ will decrease with λ, this trend supports the consistency of the radiative models that neglect scattering, which is especially relevant within the infrared spectral range that mainly contributes to radiative heat transfer in flames.

Furthermore, the "open-tip" flame E is the only one that exhibits non-zero field of σ_{λ_3} through its tip. Thus, tracking the characteristics of soot released by the flame might be considered through scattering measurements, recognizing that the signal-to-noise ratio will have to be drastically enhanced. To this end, the dynamics of the attenuation measurements will need to be specifically dedicated to the collection of scattered light coming from non-zero scattering angles [49]. Potentially, scanning the flame inwards slice by slice by

a vertical laser sheet rather than a wide beam could make the interpretation layer by layer of the scattered light at λ_3 easier.

Eventually, the green line shown for flame E in Fig. 7 addresses the sensitivity of the above evolutions of the mean local scattering coefficient to the exponent selected in Eq.(4). As an illustration of the ongoing debate about the evaluation of the soot refractive index, Kempema et al. measured a spectral dependence of the local spectral absorption coefficient in λ^{-1} at the vicinity of their ethylene flame's closed tip (see Fig. 7 in Ref. [50]). Thus, assuming from now that the exponent in Eq.(4) is equal to -1 provides with an upper bound of κ_{λ_3}, therefore a lower bound of σ_{λ_3}. As a result, the height above the burner $z/d_F \approx 5.2$ beyond which $\overline{\sigma}_{\lambda_3}$ is higher than the noise level, i.e. is significantly positive, is increased. This being said, the trends followed by $\overline{\sigma}_{\lambda_3}$ downstream $z/d_F \approx 5.2$ is then qualitatively the same, which further supports the above comments.

4. Conclusions

Probing steady laminar coflow ethylene/air non-premixed flames, the MAE technique allowed the transition at the smoke point to be documented in terms of two-dimensional fields of both soot temperature and volume fraction. In addition, the MAE technique has been specifically upgraded to obtain information at a third spectral range. Doing so, the distribution of the local spectral scattering coefficient could also be evaluated at λ_3=405 nm, showing that the non-scattering approximation is relevant within the context of radiative models in this kind of flame.

Radiative heat transfer computations used the aforementioned experi-

mental fields as inputs to gain a comprehensive understanding of the radiative quenching that leads to incomplete soot oxidation, therefore soot release through the flame tip beyond the smoke point. Thus, controlling the onset of the smoke point transition to mitigate or promote carbonaceous nanoparticles release process by such flames requires numerical simulations that decently capture the radiative quenching at the flame tip. To this end, the supplemental material S1 delivered along the present study contains the two-dimensional fields of both soot temperature and volume fraction measured. Such a dataset constitutes new high-quality experimental data for validation of soot models to complement existing temperature and soot volume fraction data taken in laminar non-premixed flames under conditions below the smoke point.

Future works will be devoted to the collection at non-zero scattering angles of light at λ_3=405 nm. This will support finer interpretation of the local spectral scattering coefficient that especially conveys soot morphological information. This additional input to the experimental characterization of the smoke point phenomenology should further sustain the development of state-of-the-art numerical simulations including models for soot morphology.

Acknowledgments

The authors feel grateful to the Centre National d'Etudes Spatiales (CNES) for its financial support under Contract No. 130615.

[1] Z. Dai, G.M. Faeth, Hydrodynamic suppression of soot formation in laminar coflowing jet diffusion flames, Proc. Combust. Inst. 28 (2000) 2085–2092.

[2] A. Jocher, H. Pitsch, T. Gomez, J. Bonnety, G. Legros, Combustion instability mitigation by magnetic fields, Phys. Rev. E 95 (2017) 063113.

[3] N. Doner, F. Liu, J. Yon, Impact of necking and overlapping on radiative properties of coated soot aggregates, Aerosol Sci. Technol. 51 (2017) 532–542.

[4] B. Franzelli, M. Roussillo, P. Scouflaire, J. Bonnety, R. Jalain, T. Dormieux, S. Candel, G. Legros, Multi-diagnostic soot measurements in a laminar diffusion flame to assess the ISF database consistency, Proc. Combust. Inst. 37 (2018) in press.

[5] F. Liu, G. Hongsheng, G.J. Smallwood, Ö.L. Gülder, Numerical modelling of soot formation and oxidation in laminar coflow non-smoking and smoking ethylene diffusion flames, Combust. Theory Modelling 7 (2003) 301–315.

[6] G. Blanquart, H. Pitsch, Analyzing the effects of temperature on soot formation with a joint volume-surface-hydrogen model, Combust. Flame 156 (2009) 1614–1626.

[7] J.-L. Consalvi, F. Liu, J. Contreras, M. Kashif, G. Legros, S. Shuai, J. Wan, Numerical study of soot formation in laminar coflow diffusion flames of methane doped with primary reference fuels, Combust. Flame 162 (2015) 1153–1163.

[8] C. Eberle, P. Gerlinger, M. Aigner, A sectional PAH model with reversible PAH chemistry for CFD soot simulations, Combust. Flame 179 (2017) 63–73.

[9] G.A. Kelesidis, E. Goudeli, S.E. Pratsinis, Flame synthesis of functional nanostructured materials and devices: Surface growth and aggregation, Proc. Combust. Inst. 36 (2017) 29–50.

[10] S. Li, Y. Ren, P. Biswas, S.D. Tse, Flame aerosol synthesis of nanostructured materials and functional devices: Processing, modeling, and diagnostics, Prog. Energy Combust. Sci. 55 (2016) 1–59.

[11] L. Mädler, H.K. Kammler, R. Mueller, S.E. Pratsinis, Controlled synthesis of nanostructured particles by flame spray pyrolysis, J. Aerosol Sci. 33 (2002) 369–389.

[12] J. Abboud, J. Schobing, G. Legros, J. Bonnety, V. Tschamber, A. Brillard, G. Leyssens, V. Lauga, E.E. Iojoiu, P. Da Costa, Impacts of oxygenated compounds concentration on sooting propensities and soot oxidative reactivity: Application to diesel and biodiesel surrogates, Fuel 193 (2017) 241–253.

[13] J. Abboud, J. Schobing, G. Legros, A. Matynia, J. Bonnety, V. Tschamber, A. Brillard, G. Leyssens, P. Da Costa, Impacts of ester's carbon chain length and concentration on sooting propensities and soot oxidative reactivity: application to Diesel and Biodiesel surrogates, Fuel 222 (2018) 586–598.

[14] S.T. Minchin, Luminous stationary flames: the quantitative relationship between flame dimensions at the sooting point and chemical composition, with special reference to petroleum hydrocarbons, J. Inst. Petrol. Technol. 17 (1931) 102–120.

[15] G.H. Markstein, J. De Ris, Radiant Emission and Absorption by Laminar Ethylene and Propylene Diffusion Flame, Proc. Combust. Inst. 20 (1984) 1637–1646.

[16] P.B. Sunderland, S. Mortazavi, G.M. Faeth, D.L. Urban, Laminar smoke points of nonbuoyant jet diffusion flames, Combust. Flame 96 (1994) 97–103.

[17] T.L. Berry Yelverton, W.L. Roberts, Effect of dilution, pressure, and velocity on smoke point in laminar jet flames, Combust. Sci. Technol. 180 (2008) 1334–1346.

[18] M.D. Smooke, C.S. McEnally, L.D. Pfefferle, R.J. Hall., M.B. Colket, Computational and experimental study of soot formation in a coflow, laminar diffusion flame, Combust. Flame 117 (1999) 117–139.

[19] C.W. Lautenberger, J.L. De Ris, N.A. Dembsey, J.R. Barnett, H.R. Baum, A simplified model for soot formation and oxidation in CFD simulation of non-premixed hydrocarbon flames, Fire Safety J. 40 (2005) 141–176.

[20] T. Beji, J.P. Zhang, W. Yao, M. Delichatsios, A novel soot model for fires: Validation in a laminar non-premixed flame, Combust. Flame 158 (2011) 281–290.

[21] N.A. Eaves, Q. Zhang, F. Liu, H. Guo, S.B. Dworkin, M.J. Thomson, Coflame: A refined and validated numerical algorithm for modeling sooting laminar coflow diffusion flames, Comput. Phys. Commun. 207 (2016) 464–477.

[22] M. Kashif, J. Bonnety, A. Matynia, P. Da Costa, G. Legros, Sooting propensities of some gasoline surrogate fuels: Combined effects of fuel blending and air vitiation, Combust. Flame 161 (2015) 1840–1847.

[23] J.-L. Consalvi, F. Liu, M. Kashif, G. Legros, Numerical study of soot formation in laminar coflow methane/air diffusion flames doped by n-heptane/toluene and iso-octane/toluene blends, Combust. Flame 180 (2017) 167–174.

[24] A. Jocher, J. Bonnety, H. Pitsch, T. Gomez, G. Legros, Dual magnetic effects on soot production in partially premixed flames, Proc. Combust. Inst. 36 (2017) 1377–1385.

[25] C.S. McEnally, L.D. Pfefferle, Sooting Tendencies of Oxygenated Hydrocarbons in Laboratory-Scale Flames, Environ. Sci. Technol. 45 (2011) 2498–2503.

[26] Q. Wang, G. Legros, J. Bonnety, C. Morin, Experimental characterization of the different nitrogen dilution effects on soot formation in ethylene diffusion flames, Proc. Combust. Inst. 36 (2017) 3227–3235.

[27] Q. Wang, G. Legros, J. Bonnety, C. Morin, A. Matynia, J.-L. Consalvi, F. Liu, Experimental assessment of the sudden-reversal of the oxygen

dilution effect on soot production in coflow ethylene flames, Combust. Flame 183 (2017) 242–252.

[28] J.H. Kent, H.Gg. Wagner, Who do diffusion flames emit smoke, Combust. Sci. Technol. 41 (1984) 245–269.

[29] R.J. Santoro, T.T. Yeh, J.J. Horvath, H.G. Semerjian, The transport and growth of soot particles in laminar diffusion flames Combust. Sci. Technol. 53 (1987) 89–115.

[30] C.M. Megaridis, R.A. Dobbins, Comparison of soot growth and oxidation in smoking and non-smoking ethylene diffusion flames, Combust. Sci. Technol. 66 (1989) 1–16.

[31] G. Legros, Q. Wang, J. Bonnety, M. Kashif , C. Morin, J.-L. Consalvi, F. Liu, Simultaneous soot temperature and volume fraction measurements in axis-symmetric flames by a two-dimensional modulated absorption/ emission technique, Combust. Flame 162 (2015) 2705–2719.

[32] G. Legros, T. Gomez, M. Fessard, T. Gouache, T. Ader, P. Guibert, P. Sagaut, J.L. Torero, Magnetically induced flame flickering, Proc. Combust. Inst. 33 (2011) 1095–1103.

[33] M. Kashif, J. Bonnety, P. Guibert, C. Morin, G. Legros, Soot volume fraction fields in unsteady axis-symmetric flames by continuous laser extinction technique, Opt. Express 20 (2012) 28742–28751.

[34] A. Jocher, H. Pitsch, T. Gomez, G. Legros, Modification of sooting tendency by magnetic effects, Proc. Combust. Inst. 35 (2015) 889–895.

[35] C.R. Shaddix, K.C. Smyth, Laser-induced incandescence measurements of soot production in steady and flickering methane, propane, and ethylene diffusion flames, Combust. Flame 107 (1996) 418–452.

[36] R. Demarco, F. Nmira, J. L. Consalvi, Influence of thermal radiation on soot production in laminar axisymmetric diffusion flames, J. Quant. Spectrosc. Radiat. Transf. 120 (2013) 52–69.

[37] F. Liu, K. A. Thomson, G. J. Smallwood, Numerical investigation of the effect of signal trapping on soot measurements using LII in laminar coflow diffusion flames, Appl. Phys. B 96 (2009) 671–682.

[38] H. Chang, T. T. Charalampopoulos, Determination of the wavelength dependence of refractive indices of flame soot, Proc. Roy. Soc. Lond. A 430 (1990) 577–591.

[39] F. Liu, K.A. Thomson, G.J. Smallwood, Soot temperature and volume fraction retrieval from spectrally resolved flame emission measurement in laminar axisymmetric coflow diffusion flames: Effect of self-absorption, Combust. Flame 160 (2013) 1693–1705.

[40] H. Zhao, B. Williams, R. Stone, Measurement of the spatially distributed temperature and soot loadings in a laminar diffusion flame using a Cone-Beam Tomography technique J. Quant. Spectrosc. Radiat. Transf. 133 (2014) 136–152.

[41] F. Goulay, P.E. Schrader, H.A. Michelsen, Effect of the wavelength dependence of the emissivity on inferred soot temperatures measured by

spectrally resolved laser-induced incandescence, Appl Phys B 100 (2010) 655–663.

[42] J. Yon, R. Lemaire, E. Therssen, P. Desgroux, A. Coppalle, K.F. Ren, Examination of wavelength dependent soot optical properties of diesel and diesel/rapeseed methyl ester mixture by extinction spectra analysis and LII measurements, Appl Phys B 104 (2011) 253–271.

[43] Y. Niko, H. Moritomo, H. Sugihara, Y. Suzuki, J. Kawamata, G.-I. Konishi, A novel pyrene-based two-photon active fluorescent dye efficiently excited and emitting in the 'tissue optical window (650-1100 nm)', J. Mater. Chem. B 3 (2015) 184–190.

[44] F. Liu, J.-L. Consalvi, A. Fuentes, Effects of water vapor addition to the air stream on soot formation and flame properties in a laminar coflow ethylene/air diffusion flame, Comb. Flame 161 (2014) 1724–1734.

[45] E.H. Chui, G. D. Raithby, P. M. J. Hughes, Prediction of radiative transfer in cylindrical enclosures with the finite volume method, J. Thermophys. Heat Transf. 6 (1992) 605–611.

[46] W.H. Dalzell, A.F. Sarofim, Optical constants of soot and their applications to heat flux calculations, J. Heat Transfer 91 (1969) 100–107.

[47] H.A. Michelsen, P.E. Schrader, F. Goulay, Wavelength and temperature dependences of the absorption and scattering cross sections of soot, Carbon 48 (2010) 2175–2191.

[48] S.A. Steinmetz, T. Fang, W.L. Roberts, Soot particle size measurements

in ethylene diffusion flames at elevated pressures, Comb. Flame 169 (2016) 85–93.

[49] T. Zhang, M. J. Thomson, Development of an improved data analysis approach for combined laser extinction and two-angle elastic light scattering diagnostics of soot aggregates, Appl. Opt. 55 (2016) 920–928.

[50] N.J. Kempema, B. Ma, M.B. Long, Investigation of in-flame soot optical properties in laminar coflow diffusion flames using thermophoretic particle sampling and spectral light extinction, Appl. Phys. B 122 (2016) 232.

List of Figures

1 Schematic of the arrangement allowing non-premixed flames to be probed by the 3C-MAE technique. Only the main items are identified. See Ref. [31] for exhaustive details of the setup. The insets on the right show typical frames when the flame and the lasers are on as captured by: (a) the "blue" camera; (b) the "red" camera; (c) the "near infrared" camera. The shadow of the central tube tip (outer diameter: 13 mm) can be seen at the bottom of each frame. 37

2 Fields of soot volume fraction (on the left of each flame's axis) and temperature (on the right) measured in flames A-E. The horizontal and vertical yellow lines indicate the axial and radial locations, respectively, of the peak soot volume fraction $f_{v,max}$ measured for each flame. For flames A and D, the white dotted contours encompass 90 % of the total soot load within the flames. Leftmost plot: profiles of mean soot volume fraction F_v (see Eq.(3)) 38

3 Populations of soot temperature/volume fraction measurements in flames A-E. The red dots, superimposed on the blue ones (whole population), highlight the specific contribution from the region of the flame located beyond z_{max}. For each flame, the temperature at the location of $f_{v,max}$ is given on the right. 39

4 Fields of radiative balance computed from the experimental fields shown in Fig. 2. The horizontal and vertical yellow lines indicate the axial and radial locations, respectively, of the peak soot volume fraction $f_{v,max}$ measured for each flame. Every contour delineated by a white solid line encompasses the zone that produces 90 % of the radiative power attributed to soot. For flame E, the circles delineate the equivalent contour that is obtained when the data of Dalzell and Sarofim [46] are used to infer the spectral dependence of κ_λ in Eq.(2). Starting from the upper height of the aforementioned contour in flames D and E, the white dotted line indicates the outer locations of 5% of the peak radiative balance, showing the transition from a close-tip to an open-tip flame in the distribution of radiative balance. 40

5 Correlations between the relative consumtion rate and the radiative power along the height above the burner z cumulated from the location of $F_{v,max}$. Along the trend lines drawn for flames (A-E), a set of F_v levels are indicated by the color circles. 41

6 Lower row: evolution along z/d_F in flames A-E of the ratios $\beta_{\lambda_3}^{peak}(z)/\kappa_{\lambda_2}^{peak}(z)$. The opacity of the circles is proportional to both relative levels of $\kappa_{\lambda_2}^{peak}(z)$ and $\beta_{\lambda_3}^{peak}(z)$. The red and blue lines indicate the values of $\kappa_{\lambda_3}^{peak}(z)/\kappa_{\lambda_2}^{peak}(z)$ predicted by Michelsen et al. [47] and the Rayleigh limit, respectively. Upper row: profiles of measured $\beta_{\lambda_3}(r)$ (blue line) and estimated $\kappa_{\lambda_3}(r)$ (red line) at z/d_F=6 for flame E (left y-axis). Subtracting the latter from the former leads to the profile of $\sigma_{\lambda_3}(r)$ (black line and right y-axis). β_λ, κ_λ, and σ_λ are all shown in mm^{-1}. 42

7 Evolution along z/d_F in flames A-E of the mean local extinction (black lines and lower x-axis) and scattering (red lines and upper x-axis) coefficients evaluated within the blue spectral range. For a given flame, the part in solid line indicates the region of the flame that covers 90% of the radiative power attributed to soot (see the white contours in Fig. 4). For flame E, the green line represents the mean local scattering coefficient evaluated as the exponent in Eq.(4) is assumed to be -1. 43

Table 1: Identification of the conditions investigated. All flames are established at atmospheric pressure and for an air flow rate of 60 L.min^{-1}. Flow rates are given at atmospheric pressure and room temperature (293 K).

Flame	A	B	C	D	E
Fuel flow rate (L.min^{-1})	0.191	0.210	0.229	0.239	0.248

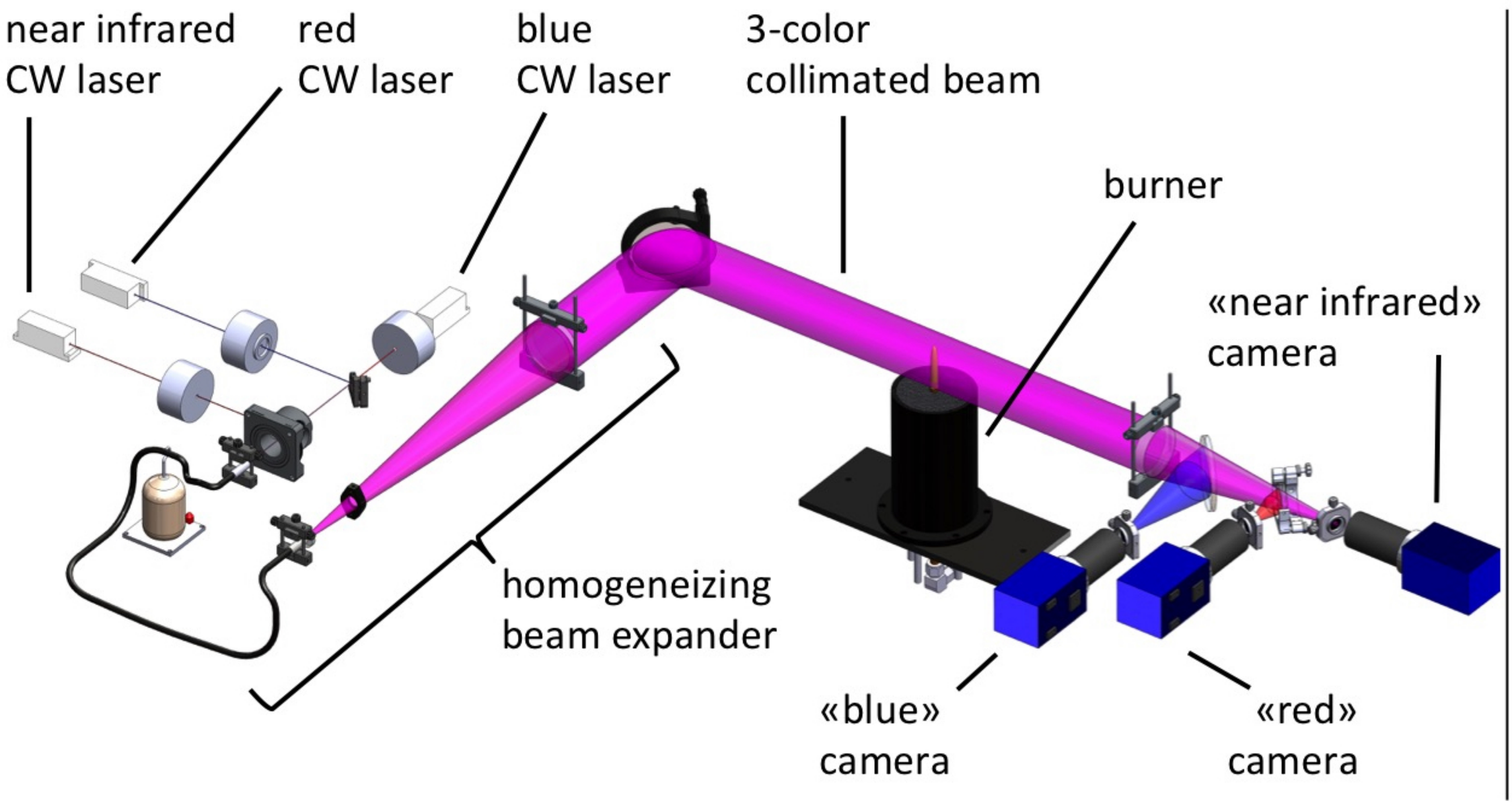
near infrared
CW laser
red
CW laser
blue
CW laser
3-color
collimated beam
burner
«near infrared»
camera
homogeneizing
beam expander
«blue»
camera
«red»
camera

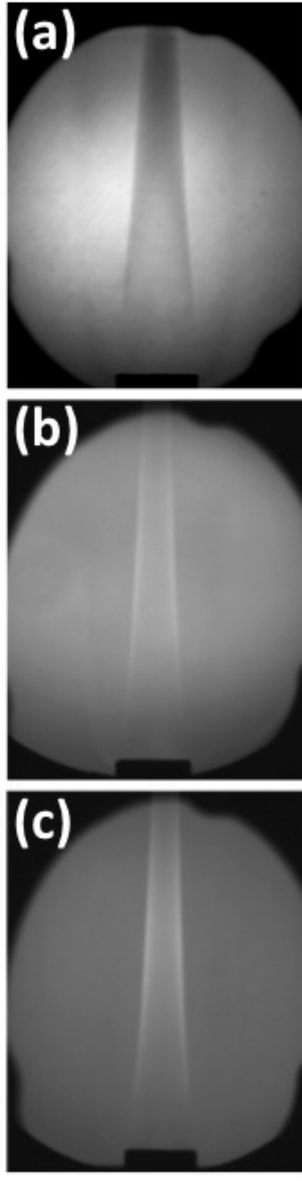
(a)
(b)
(c)

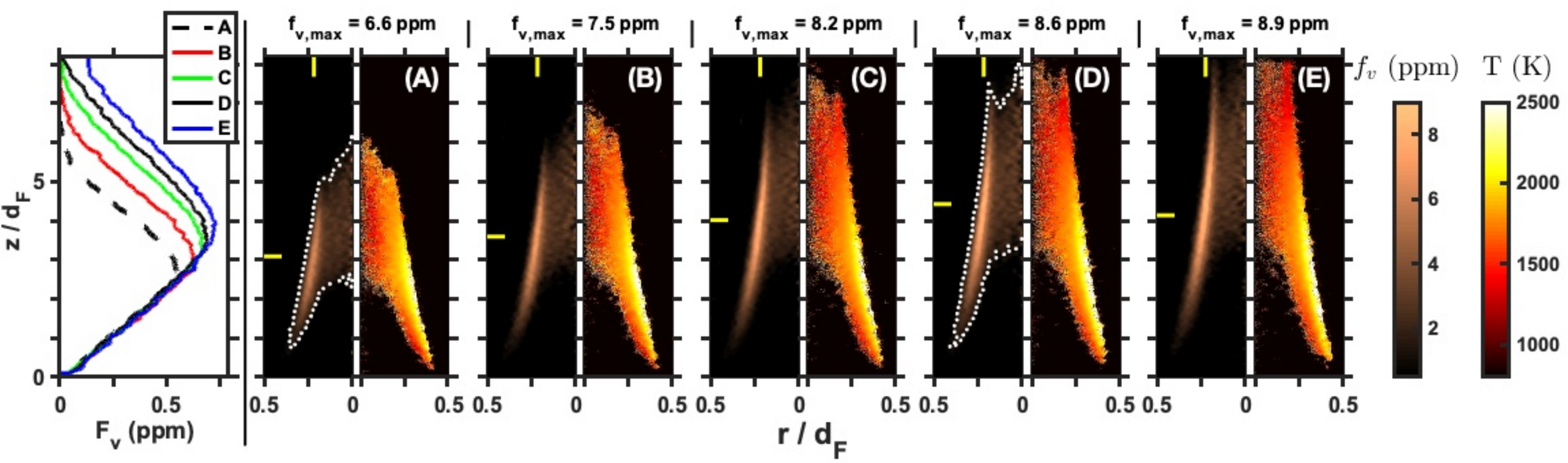
A
B
C
D
E
$f_{v,max}$ = 6.6 ppm
$f_{v,max}$ = 7.5 ppm
$f_{v,max}$ = 8.2 ppm
$f_{v,max}$ = 8.6 ppm
$f_{v,max}$ = 8.9 ppm
(A)
(B)
(C)
(D)
(E)
f_v (ppm)
T (K)
2500
2000
1500
1000
8
6
4
2
z / d_F
F_v (ppm)
r / d_F
0
0.5
5

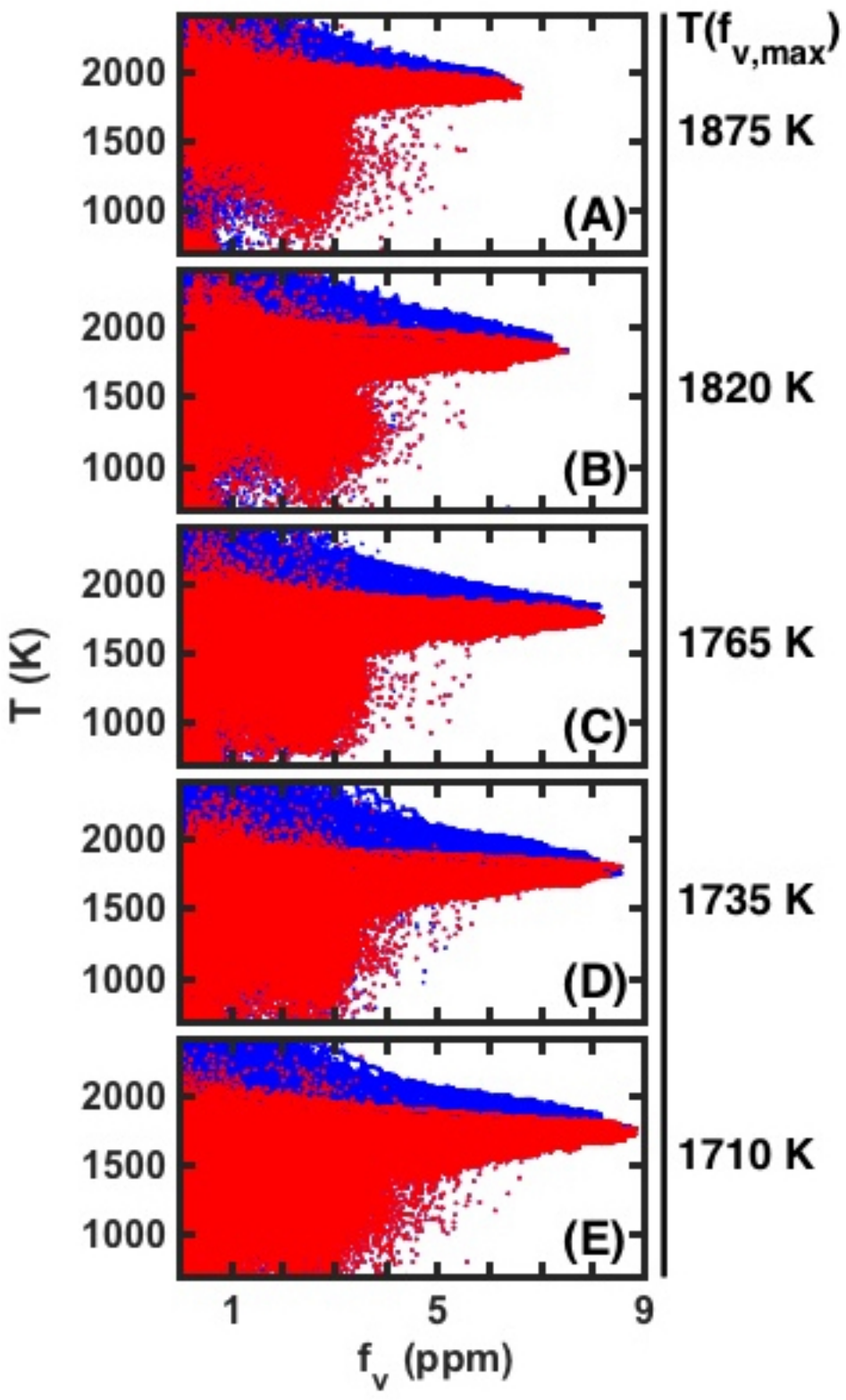
T(f_v,max)
1875 K
1820 K
1765 K
1735 K
1710 K
(A)
(B)
(C)
(D)
(E)
2000
1500
1000
T (K)
1
5
9
f_v (ppm)

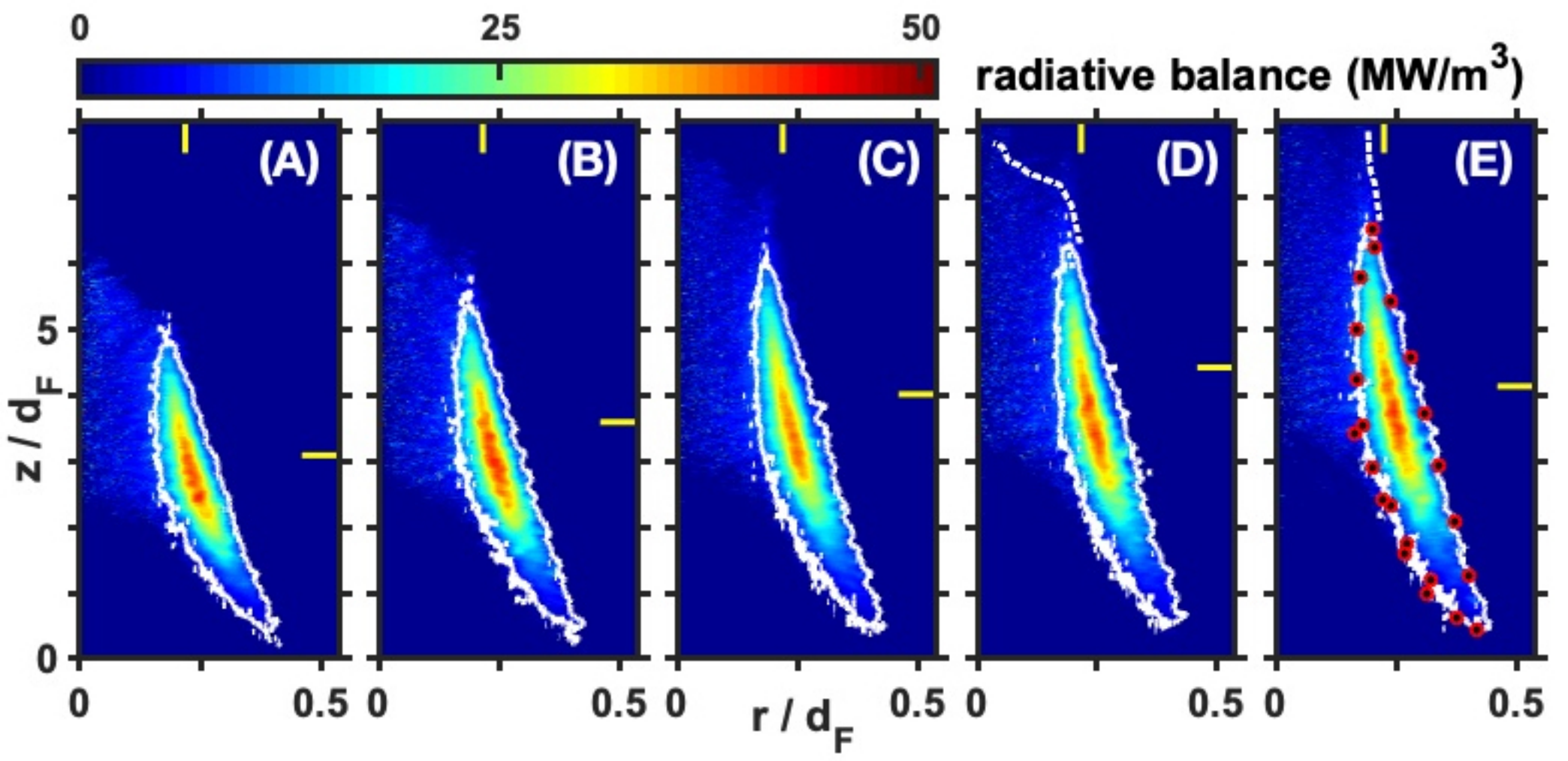
0
25
50
radiative balance (MW/m3)
(A)
(B)
(C)
(D)
(E)
z / dF
r / dF
0
5
0.5

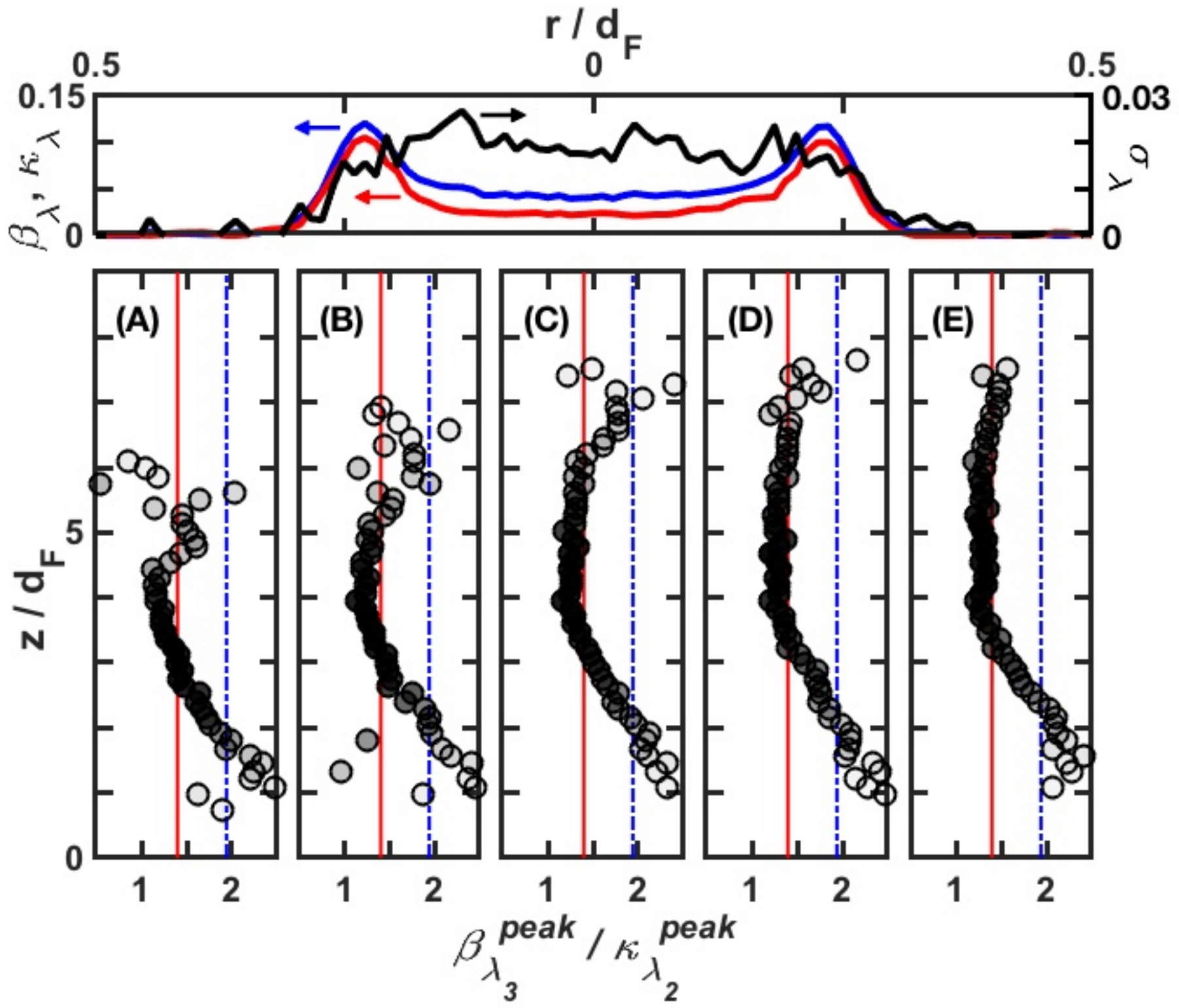
r / d_F
0.5
0
0.5
0.15
0
0.03
0
β_λ, κ_λ
σ_λ
(A)
(B)
(C)
(D)
(E)
z / d_F
5
0
1
2
β_λ3 peak / κ_λ2 peak

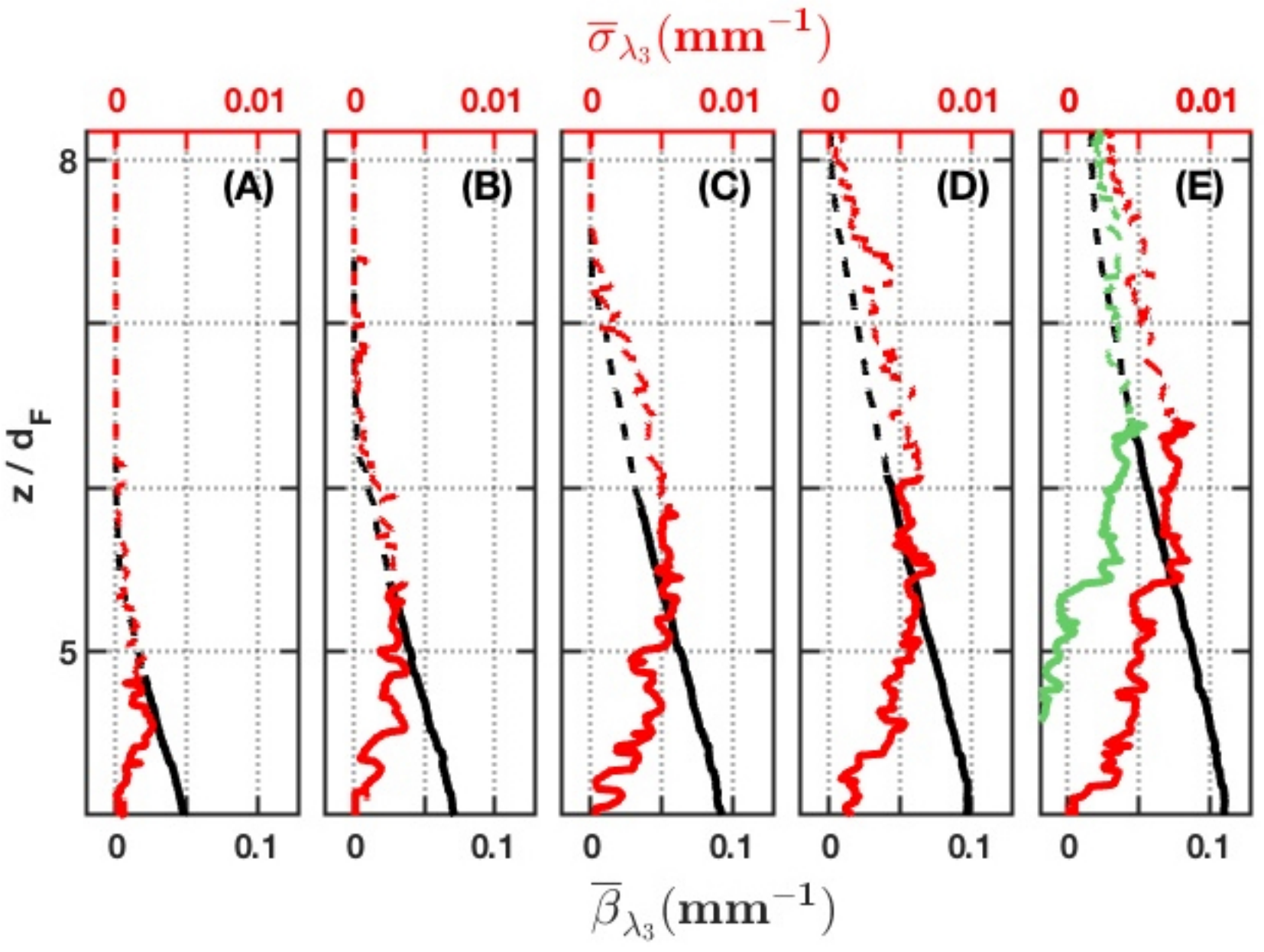
$\overline{\sigma}_{\lambda_3}(\mathrm{mm}^{-1})$
0
0.01
(A)
(B)
(C)
(D)
(E)
8
5
z / d_F
0
0.1
$\overline{\beta}_{\lambda_3}(\mathrm{mm}^{-1})$